JOURNAL OF MATERIALS SCIENCE 16 (1981) 1039–1051

Thermal ageing effects in AISI type 316 stainless steel

L. P. STOTER*
H. H. Wills Physics Laboratory, Royal Fort, Tyndall Avenue, Bristol, UK

The effects of long-term thermal ageing on the microstructure of AISI type 316 stainless steel are described. The microstructure of the aged steel is related to the reported embrittlement of the steel. The precipitation found is complex and the embrittlement appears to result, in part, from specimen preparation techniques interacting with the microstructure. The dominant creep deformation mechanism under service conditions appears to be diffusion creep.

1. Introduction

The exposure of AISI type 316 stainless steel to relatively high temperatures (~ 650° C) for long periods results in a deterioration of the mechanical properties, principally a loss of ductility. An understanding of this ageing process can only come from a detailed knowledge of the microstructural developments. This paper reports on a study of the microstructure of two samples of type 316 steel, aged at about 650° C for 28 000 and 60 000 h in service and on a solution-treated sample. The material was provided by the Central Electricity Generating Board, Berkeley Nuclear Laboratory (CEGB, BNL), who had previously used it in an extensive mechanical test programme. Some of their results are included here to allow a complete discussion of the ageing of type 316 steel.

As this paper shows, the microstructure of long-term, thermally-aged type 316 steel is extremely complex. For example, eighteen different precipitate phases were found. This complexity has necessarily led to the microstructure being studied in a selective way and only those features of the microstructure considered important in the ageing process received detailed attention.

2. Experimental procedure

Details of the specimen histories and compositions are given in Tables I and II. The additional heat treatment of Specimen C provided a specimen with the same composition as Specimen A but with the mechanical properties and microstructure of unaged material.

Thin foils for transmission electron microscopy (TEM) study were prepared from the bulk material by spark cutting, grinding and mechanical polishing and finally jet polishing to perforation using a Struers Tenupol set at 40 volts with a 10% perchloric acid in glacial acetic acid electrolyte at room temperature.

Carbon extraction replicas for TEM study were taken from polished sections and fracture surfaces. The polished sections were lightly etched with a 5% bromine in methanol solution before carbon coating. Fracture surfaces were prepared by cooling a suitably-shaped, notched piece of material to liquid nitrogen temperature and then striking it. After carbon coating using standard evaporator equipment, the carbon films were removed electrolytically using a 10% hydrochloric acid in methanol electrolyte, a carbon electrode and a potential of about 2 volts. The carbon films were supported on copper grids.

TABLE I Specimen histories

Specimen	Time (h)	Temperature (° C)	Stress ($MN\,m^{-2}$)
A	2.6×10^4	650	36
B	6×10^4	640	36
C	as A but plus 1 h at 1050° C		

---

*Present address: Department of Metallurgy and Science of Materials, University of Oxford, Parks Road, Oxford, UK.

0022–2461/81/041039–13$03.30/0 © *1981 Chapman and Hall Ltd.*

TABLE II Specimen compositions (wt %)

Element	AISI 316 specification	Specimen A	Specimen B
C	0.08 max.	0.06	0.07
S	0.030 max.	0.014	0.012
P	0.045 max.	0.028	0.024
Mn	2.0 max.	1.41	1.51
Si	1.0 max.	0.56	0.65
Ni	10–14	11.0	11.1
Cr	16–18	16.5	16.1
Mo	2–3	2.43	2.43
Ti	–	< 0.05	< 0.05
Nb	–	< 0.1	< 0.1
Cu	–	0.17	0.14
V	–	–	–
B	–	90 ppm	90 ppm
Fe	balance	balance	balance

Some of the fracture surfaces were examined by scanning electron microscopy (SEM) and in addition specimens were prepared specifically for SEM study by ion etching mechanically-polished surfaces using an Edwards IBT 200 ion thinner, running on argon. TEM analysis was performed on a Philips EM400 fitted with STEM pole-pieces and an energy dispersive X-ray (EDX) detector. Initial identification of unknown phases was carried out using convergent beam diffraction [1] and EDX analysis. Although EDX analysis was only used qualitatively, the combination with convergent beam diffraction methods proved very powerful. Subsequent identification of phases was accomplished using the EDX analysis alone to provide a "fingerprint". This was a fast and, in the case of carbon extraction replicas, reliable method, no confusion occurring between the different phases studied, although this may not be generally true. The spectra of given phases remained substantially constant, allowing any variations to be taken as genuine.

The study of various surfaces was carried out be SEM on a Cambridge Stereoscan S2 and an S4, the latter fitted with an EDX detector.

The mechanical test programme conducted by BNL consisted of a variety of tensile, creep and fatigue tests using standard methods. Specimens were generally prepared in strip form by machining and punching. Note that some were particularly thin (0.75 mm).

In addition to the mechanical testing conducted by BNL, tests were carried out to study the effects of specimen preparation methods on the mechanical behaviour of the material. These consisted of straining two bars fabricated from Specimen A in a small four-point bending machine and observing the behaviour of the surfaces in the SEM. The two bars were identical except that Bar I had one long face prepared by machining and mechanical polishing while the equivalent face of Bar II was prepared by spark cutting, mechanical polishing and electropolishing.

3. Results

3.1. Microstructures

Summaries of the specimen microstructures and the crystallography of some of the phases encountered are given in Tables III and IV. In addition some eight other phases were found varying from diamond to titanium dioxide and complex amorphous phases containing such elements as Al, Ca, Cr, K, Mn, S, Si and Ti, most of which were present only in very small amounts, often only single particles. EDX spectra for the more common phases are shown in Fig. 1. The boride, M_2B, was not in fact found in the specimens reported on in this paper but in a related austenitic steel and is included here because of the very close similarity between its EDX spectrum and that of molybdenum-deficient $M_{23}C_6$. However, the two phases can easily be distinguished using diffraction techniques.

A number of phases found were obviously unimportant in the process of ageing and embrittlement since they were present in similar amounts in both the ductile, solution-treated Specimen C an in the brittle, aged Specimens A and B. These include the complex amorphous phases which may also be discounted because of their extreme rarity. Also included are alumina, silicon carbide and diamond which, although somewhat more common, were found only in carbon extraction replicas from polished sections and are almost certainly artefacts from the preparation processes. Manganese sulphide and spinel particles were common in all three specimens, the manganese sulphide as long stringers produced during the original steel production processes. The technique of ion etching revealed that there were often large voids closely associated with both of these types of inclusion (Fig. 2) and indeed some were in fact hollow, as seen on the replicas (Fig. 3). In the case of the ductile, solution-treated Specimen C, which failed transgranularly, the manganese sulphide stringers were closely associated with the liquid nitrogen

TABLE III

Specimen	$M_{23}C_6$	Laves	M_6C	Ferrite
A In service 28 000 h	Large amounts of small cubes and plates at ig*. Nearly continuous sheets at gb†.	Not found.	Always associated with large $M_{23}C_6$ in gb or at triple junctions.	Large, irregular blocks and continuous sheets at gb.
B In service 60 000 h	Some small cubes and plates at ig. Nearly continuous at gb.	Some irregular blocks at gb. Very large amounts at ig. Associated with $M_{23}C_6/M_6$ at gb.	Always associated with large $M_{23}C_6$ in gb or at triple junctions.	Not found.
C Re-solution treated	Some irregular, coherent blocks at gb.	Not found.	Not found.	Not found.

*ig intragranular sites.
†gb grain boundaries.
Note: (i) Slag particles, consisting of MnS and spinel were present in all specimens. (ii) Numerous, rare types of particle have been found in all specimens.

fracture surfaces (Fig. 4) and would appear to be the cause of failure. In the aged, brittle specimens, Specimens A and B, there was also evidence of distinct precipitate-free zones surrounding the manganese sulphide stringers (Fig. 5).

The phases considered important in the development of the microstructure consist of $M_{23}C_6$, M_6C, Laves and ferrite. $M_{23}C_6$ only occurred as a small number of coherent grain boundary precipitates in Specimen C while the others were absent. Large quantities of $M_{23}C_6$ and small amounts of M_6C and ferrite were present in Specimen A. Large amounts of $M_{23}C_6$ and Laves, but no ferrite and only small amounts of M_6C, were present in Specimen B. The phases present only in small quantities, M_6C and ferrite, were always found in association with Laves or $M_{23}C_6$. The morphologies and incidences of these four phases are summarized in Table III.

$M_{23}C_6$ occurred in all three specimens and in a

TABLE IV

Phase	Lattice type	Point group	Space group	Lattice parameters (nm)
Austenite	f c c	m3m	*F*m3m	$a = 0.3598$
Ferrite	b c c	m3m	*I*m3m	$a = 0.2866$
$M_{23}C_6$	f c c	m3m	*F*m3m	$a = 1.0569$
M_6C	Diamond	m3m	*F*d3m	$a = 1.095$
Laves	Hexagonal	6/mmm	$P6_3$/mmc	$a = 0.473$ $c = 0.772$
M_2B	Orthorhombic	mmm	*F*ddd	$a = 1.457$ $b = 0.732$ $c = 0.422$
Spinel	Diamond	m3m	*F*d3m	$a = 0.851$
Alumina	Trigonal	$\bar{3}$m	$R\bar{3}$c	$a = 0.4759$ $c = 1.2991$
Manganese sulphide	f c c	m3m	*F*m3m	$a = 0.5224$
Silicon carbide	Hexagonal	6mm	$P6_3$mc	$a = 0.3076$ $c = 0.5048$

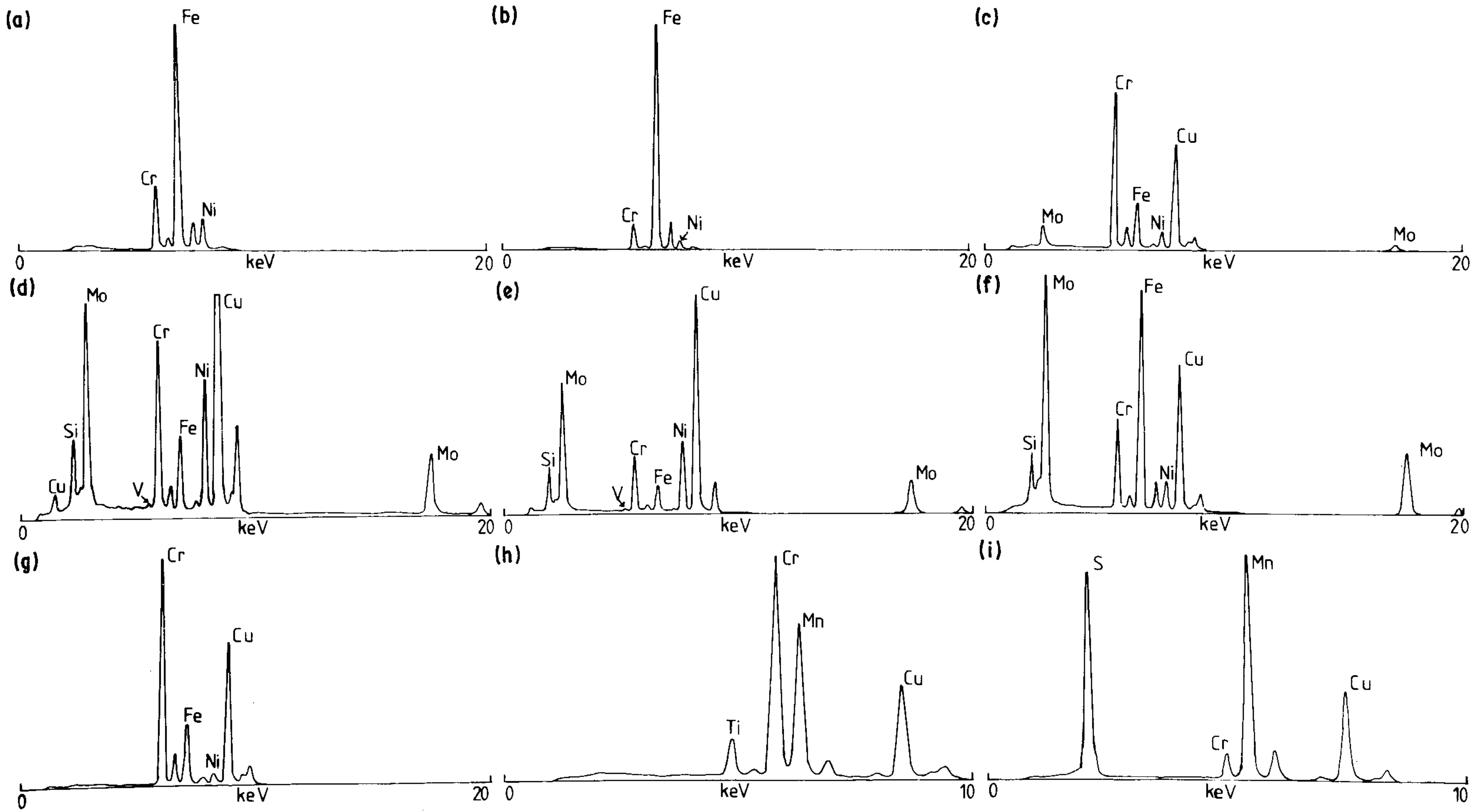

Figure 1 EDX spectra from (a) austenite, (b) ferrite, (c) $M_{23}C_6$, (d) M_6C, (e) M_6C, (f) Laves, (g) M_2B, (h) spinel and (i) MnS. Note Cu peak due to specimen support grid.

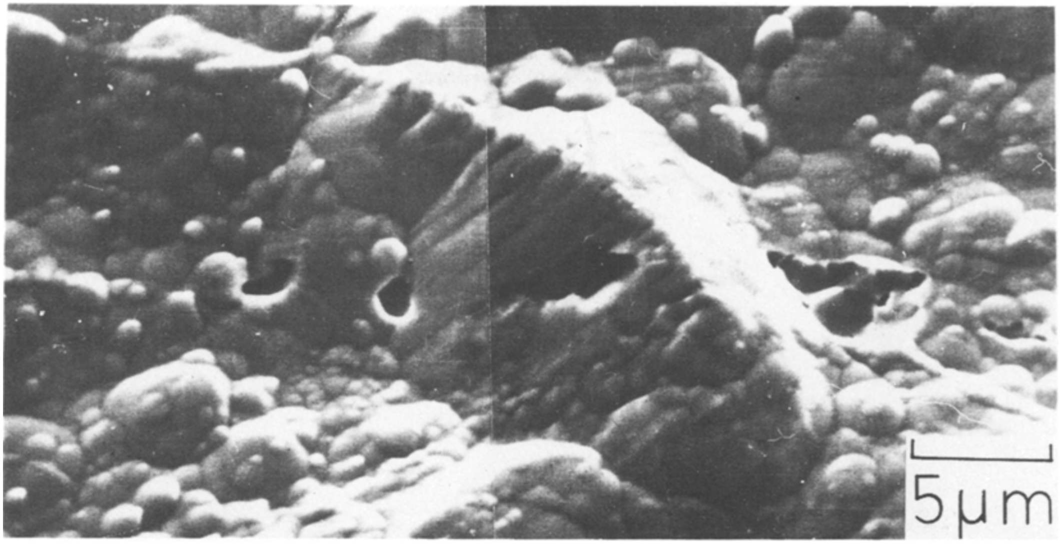

Figure 2 Voids associated with MnS and spinel, as revealed by ion etching.

wide variety of morphologies in Specimens A and B. In Specimen C, the solution-treated material, it was present only in small quantities as semi-coherent particles, about 100 nm across, on grain boundaries only. However, in the aged material considerable quantities of $M_{23}C_6$ were present both intragranularly and intergranularly. In both Specimens A and B two intergranular morphologies were present. One type consisted of small particles, about 100 nm across, and cubic in appearance although they have in fact been shown to be octahedra [2]. The other type consists of thin, needle-like, plates generally a few micrometres long, 200 to 300 nm across and a few tens of nanometres thick.

The morphology of $M_{23}C_6$ growing on the grain boundaries was considerably more varied and a number of varieties are shown in Fig. 6. The size and shape varies from small, cubic particles to large, irregular particles and the density varies from widely-space to almost continuous sheets. No relationship between grain boundary orientations and precipitate morphology was found except for twin boundaries where the precipitation was either very dense, semi-coherent and growing into both

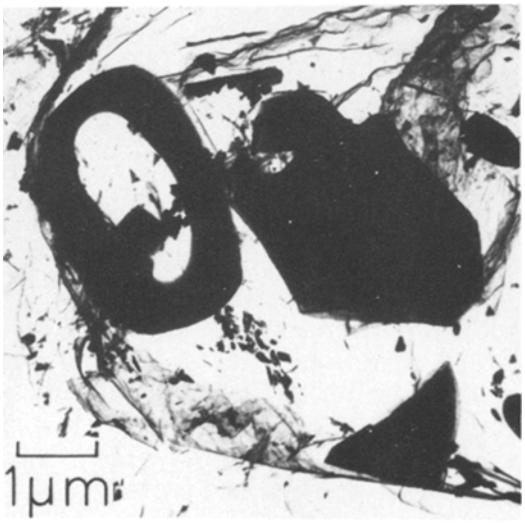

Figure 3 Hollow MnS particles.

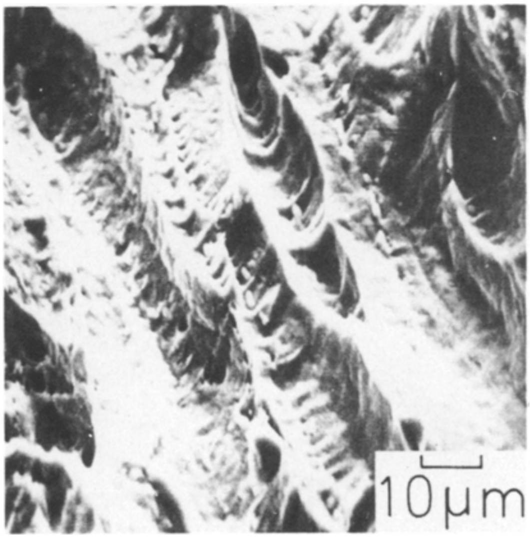

Figure 4 Fracture surface from solution-treated material, showing ductile fracture. Note MnS particles.

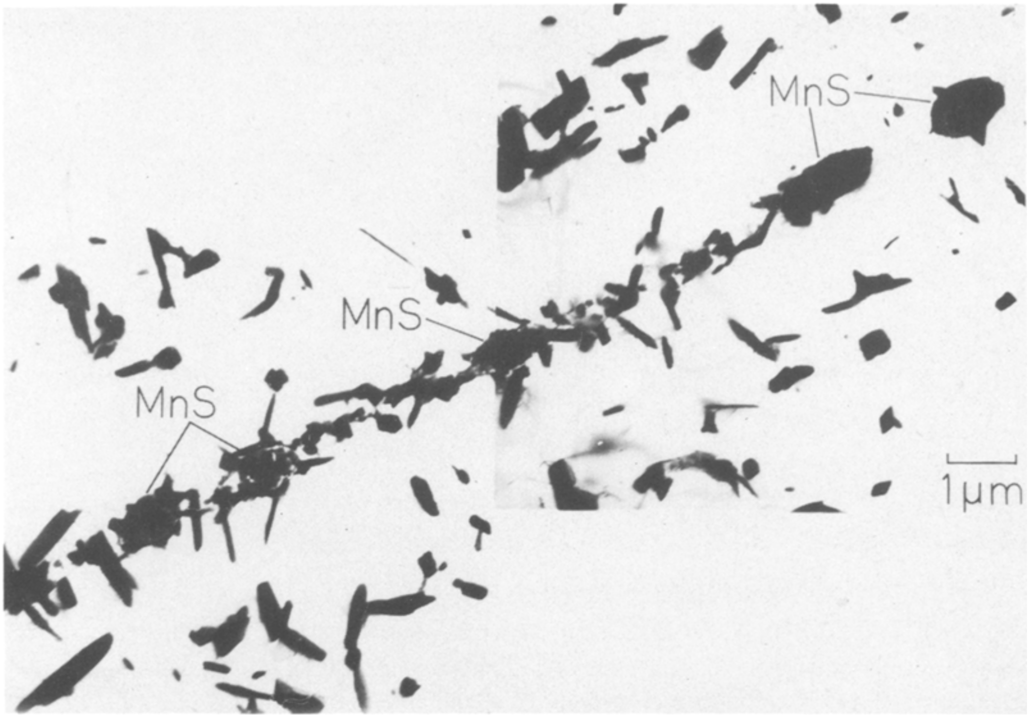

Figure 5 Precipitate denuded zone adjacent to MnS.

grains, or very sparse, being very similar to the general intragranular precipitation. Although not proved, these probably constitute incoherent and coherent twin boundaries, respectively.

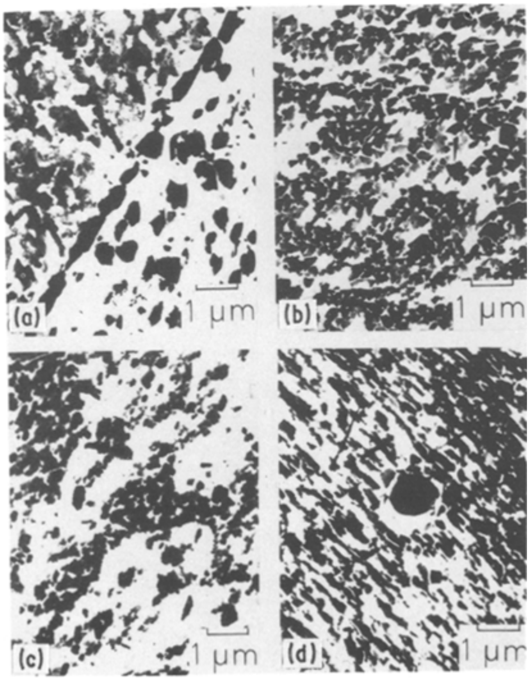

Figure 6 Various morphologies of $M_{23}C_6$ grain boundary precipitation.

The above observations apply to both Specimens A and B. However, while $M_{23}C_6$ was the only phase precipitating in large amounts in Specimen A, there were also large quantities of Laves phase in Specimen B. In the grains about 90% of the precipitation was Laves and 10% $M_{23}C_6$, while in the grain boundaries about 75% of the precipitation was $M_{23}C_6$ and 25% Laves, except for twin boundaries which contained no Laves. The Laves phase was always faulted, often very densely, and grew in an elongated, rounded, often multi-lobed form. Laves tended to nucleate on $M_{23}C_6$ and in the grains the nucleus was a small cube-like $M_{23}C_6$ particle (Fig. 7). However, intragranular Laves particles were often found with no $M_{23}C_6$ nucleus, although the lower level of intragranular $M_{23}C_6$ in Specimen B compared with Specimen A suggests that much of the $M_{23}C_6$ has dissolved.

Ferrite and M_6C occurred only in association with $M_{23}C_6$ and Laves. Ferrite was present only in Specimen A, occurring either as continuous sheets on each side of the $M_{23}C_6$ grain boundary precipitation, forming a sandwich, or as single particles growing out of the $M_{23}C_6$ grain boundary precipitation into the austenite matrix (Fig. 8).

M_6C was found in both Specimens A and B, always in association with $M_{23}C_6$. Generally the

Figure 7 Laves phase precipitate with $M_{23}C_6$ nucleus.

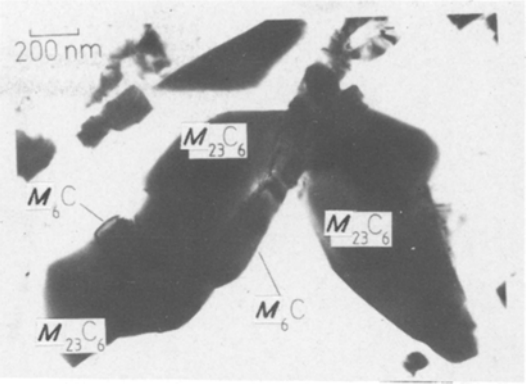

Figure 9 Mixed $M_{23}C_6/M_6C$ precipitate from Specimen A.

associated $M_{23}C_6$ particles were unusually large. In Specimen A the M_6C was inter-grown with the $M_{23}C_6$ (Fig. 9) and in Specimen B the M_6C occurred with Laves as a feathery growth surrounding the large, central $M_{23}C_6$ particle (Fig. 10). In these mixed phase particles the $M_{23}C_6$ was slightly depleted in nickel, although generally the $M_{23}C_6$ composition was remarkably constant. However, the M_6C composition was very variable, as shown in Fig. 1, although interestingly there was always about 1% vanadium present. Vanadium was found nowhere else in the specimens and was present overall at a level of less than 0.1%. M_6C was found in a number of other mixed phase precipitates, but always as a minor component.

EDX revealed no segregation in the austenite matrix. However, thin foils revealed a slight degree of preferential etching of grain boundaries (Fig. 11) and bend contours along the grain boundaries suggest the presence of strain. This was confirmed by convergent beam diffraction patterns (Fig. 12) which show a blurring and small shift of the fine detail near to the grain boundaries.

The general dislocation density in the austenite was low except adjacent to some grain boundaries,

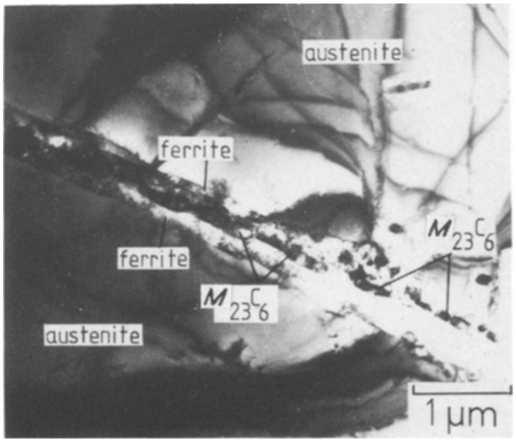

Figure 8 Ferrite in Specimen A.

Figure 10 Mixed $M_{23}C_6/M_6C$/Laves precipitated from Specimen B.

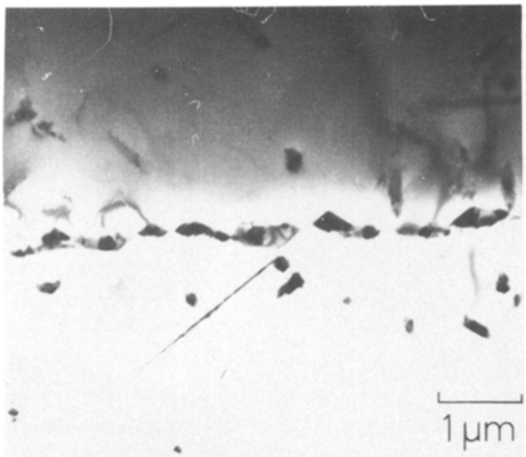

Figure 11 Grain boundary in thin foil from Specimen A. Note preferential etching and bend contours along boundary.

which contained several times more dislocations (Fig. 13) and in coherent twin boundaries which contained similar numbers of dislocations (Fig. 14).

In addition to the large voids associated with manganese sulphide and spinel, a number of small voids, always associated with precipitates, were found in both Specimens A and B (Fig. 15) in the grain boundaries and the grains.

3.2. Mechanical properties

A number of observations on the mechanical properties of the material, in addition to the BNL programme, formed a minor part of the study. It was noted that in general, straining of the aged material produced extensive grain boundary cracking in the surface (Fig. 16), an observation also made by BNL in tensile and creep tests.

When preparing fracture surfaces at liquid nitrogen temperatures the solution-treated Speciment C was more ductile and more difficult to fracture than either of the thermally-aged specimens. This difference was strongly reflected in the nature of the fracture surfaces, as seen in the SEM. The aged Specimens A and B, exhibited a generally intergranular, brittle fracture surface (Fig. 17), although some areas of ductile fracture were present while the solution-treated Specimen C presented a wholly fibrous, ductile fracture surface, closely associated with MnS stringers (Fig. 3).

In attempting to produce grain boundary failure in the specimen surfaces, it was discovered that the way in which the surface was prepared was very important. Four-point bending tests were carried out using small bars fabricated from Specimen A. Typical SEM micrographs of the surfaces are shown in Fig. 18 where a surface strain of about 6 to 7% has been set. Bar I, with the machined and mechanically-polished surface, developed slip bands at an early stage (~ 4.5% surface strain) and, with increasing strain, voids appeared along the slip bands and at their intersection with grain boundaries. At the highest strain (~ 9% surface strain) a second system of

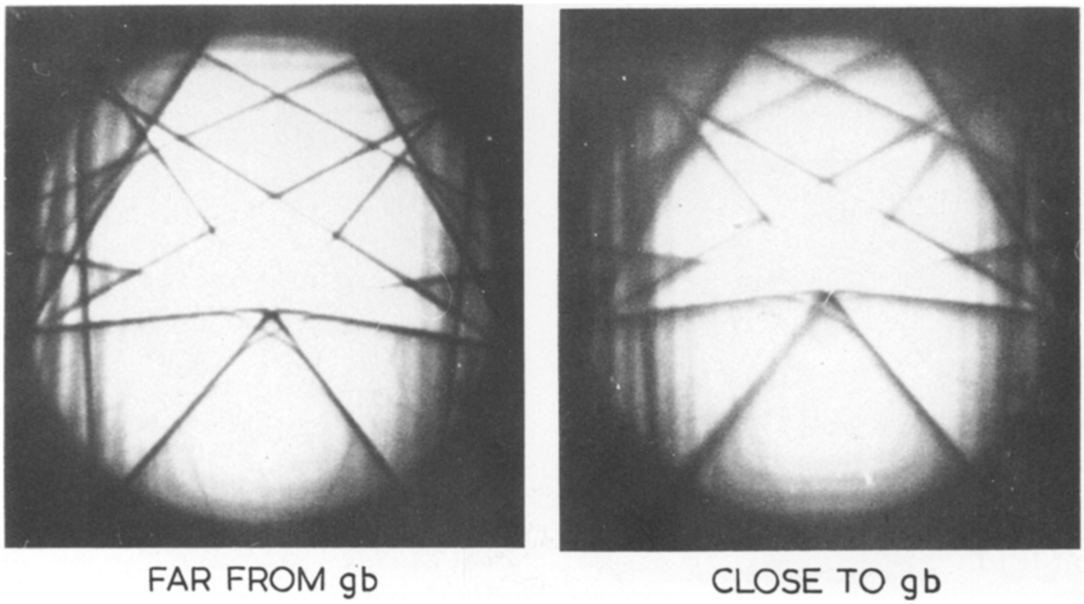

Figure 12 Convergent beam diffraction patterns revealing strain near grain boundary (gb) of Fig. 11.

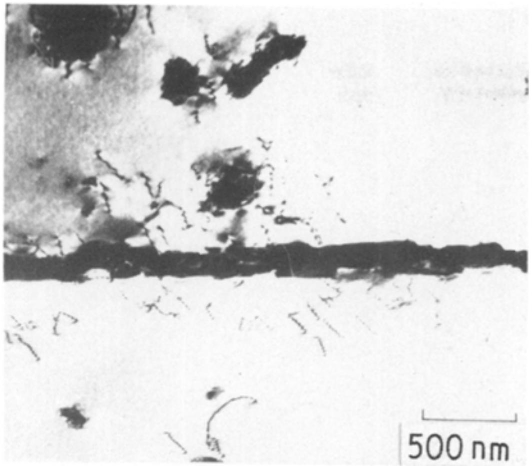

Figure 13 High dislocation density near to a grain boundary.

slip bands appeared. In contrast, Bar II with the spark-cut, mechanically-polished and electropolished surface, did not develop slip bands until higher strains were reached (~ 6% surface strain) and then they were very fine. The voidage was considerably reduced and a second system of slip bands did not develop, even at the highest strains (~ 10% surface strain).

4. Discussion

4.1. Precipitation

Precipitation of intermetallic phases, particularly of the sigma phase, is often associated with embrittlement, although not inevitably [3, 4]. The complete absence of sigma phase from both of the embrittled specimens was a somewhat unexpected result. Consideration of specimen preparation and examination techniques and their comparison with the methods of other workers led to the conclusion that the observation was genuine. Results from other workers [5] suggest that for alloys of the composition of Specimens A and B ageing for long periods at about 650° C will favour the formation of Laves phase in preference to sigma phase. The explanation probably lies in the level of carbon, high carbon levels (> 0.04 wt%) apparently preventing the formation of sigma and chi phases [5]. Laves phase and particularly the highly faulted form found in Specimen B might be able to incorporate relatively large amounts of carbon.

Consideration of the iron/chromium/nickel phase diagram for 650° C shows that the composition of type 316 steel is close to the $\gamma/\gamma + \alpha$ phase boundary. Thus small, local variations in chromium or carbon levels, caused by rapid $M_{23}C_6$ precipitation, could easily lead to the formation of ferrite.

The presence of M_6C is particularly interesting. Although occurring in only small amounts, its widespread distribution in Specimens A and B, unlike the ferrite, suggests that it is of some significance in the precipitation process. This suggestion is strengthened by several factors;

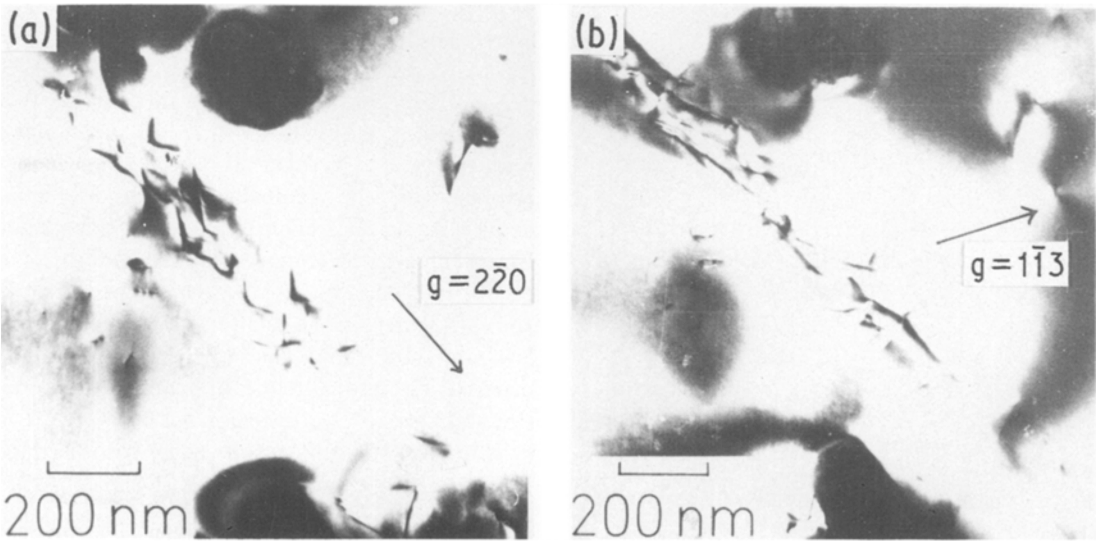

Figure 14 Coherent twin boundaries. Note dislocations in boundaries.

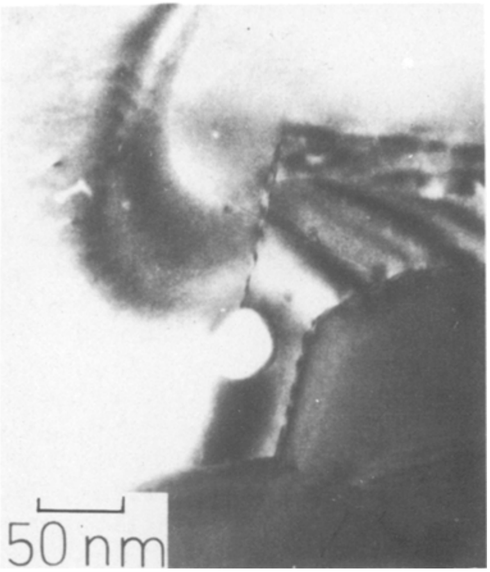

Figure 15 Voids associated with precipitates in thin foils.

M_6C always occurred in association with other precipitates, always contained a trace of vanadium, only occurred on grain boundaries and usually affected the morphology of the associated phases.

The spinel and manganese sulphide inclusions are almost certainly unimportant in the process of embrittlement, since they occur in all three specimens. However, the manganese sulphide stringers appear to nucleate failure in Specimen C, the solution-treated, ductile specimen, as can be seen from the fracture surfaces (Fig. 3). Their absence from the fracture surfaces of Specimens A and B indicates a different failure mechanism.

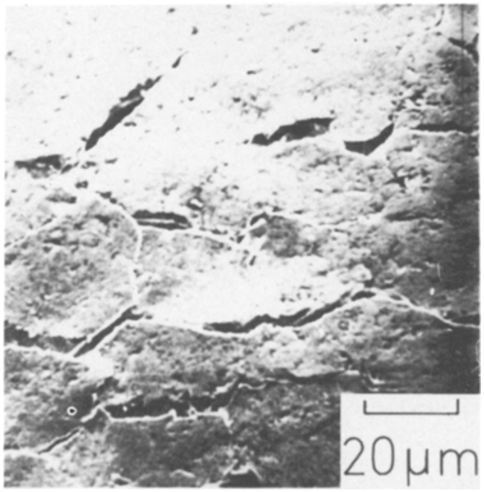

Figure 16 Failure of grain boundaries at the surface of strained material.

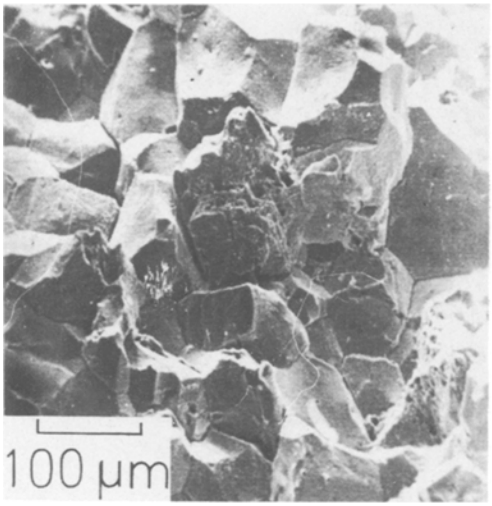

Figure 17 Fracture surface from aged material.

4.2. Deformation mechanisms

The difference between creep under service conditions (see Table I) and under accelerated creep test conditions (see Table V) needs emphasis. The considerable differences in applied stress make it unlikely that the same creep mechanisms have operated in both cases. Thin foils from accelerated creep test specimens show very high dislocation densities (Fig. 19) whereas the aged material shows a general dislocation density some 10^3–10^4 times lower. Some of this difference may be accounted for by absorption of dislocations into interfaces but it seems unlikely that this could account completely for the difference. Coherent twin boundaries are considered to provide a good record of dislocation activity [6] and in the aged material the dislocation density in coherent twin boundaries is indeed some 5 to 10 times higher than the general dislocation density. This is comparable with the anomalously high dislocation density found adjacent to some grain boundaries. However, this still represents a considerably lower dislocation density than the creep tested material and the conclusion is that there has been a low level of dislocation activity in the serviced material. The large amounts of precipitation in this material indicate that diffusion has been active.

Estimates of the strain rates for Herring–Nabarro (H–N) creep [7], Coble (C) creep [8] and dislocation creep were made for the service conditions of 650° C and 36 MVm^{-2} stress. The values obtained were (see appendix):

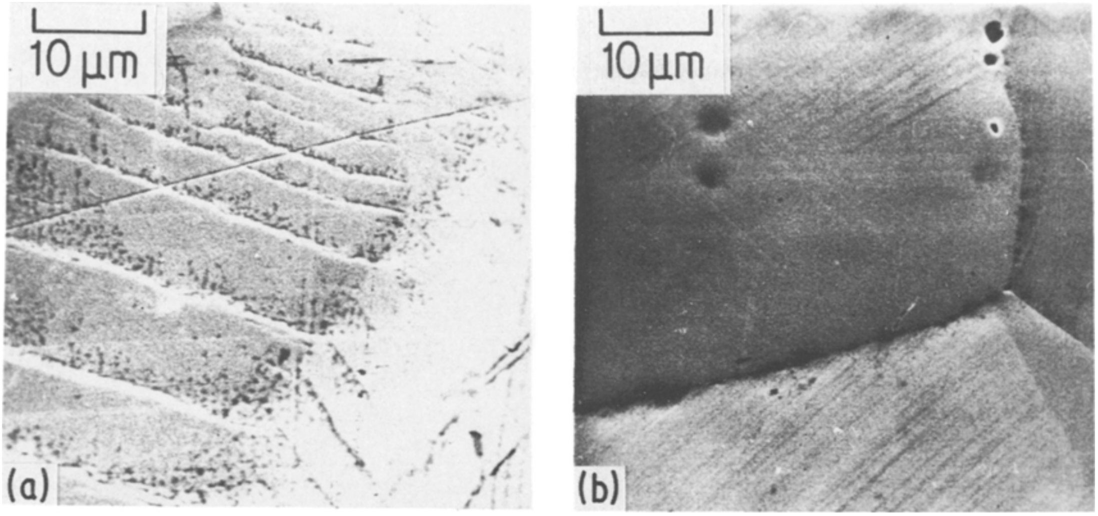

Figure 18 The surface of bent bars (a) machined and mechanically polished, (b) spark-cut, mechanically polished and electropolished.

$\dot{\epsilon} = 7.36 \times 10^{-12}\ \text{sec}^{-1}$, dislocation creep;
$\dot{\epsilon} = 8.3 \times 10^{-11}\ \text{sec}^{-1}$, H–N creep;
$\dot{\epsilon} = 1.0 \times 10^{-9}\ \text{sec}^{-1}$, C creep.

Thus it would appear that while dislocation creep is dominant under accelerated creep test conditions, under service conditions Coble creep is the dominant mechanism.

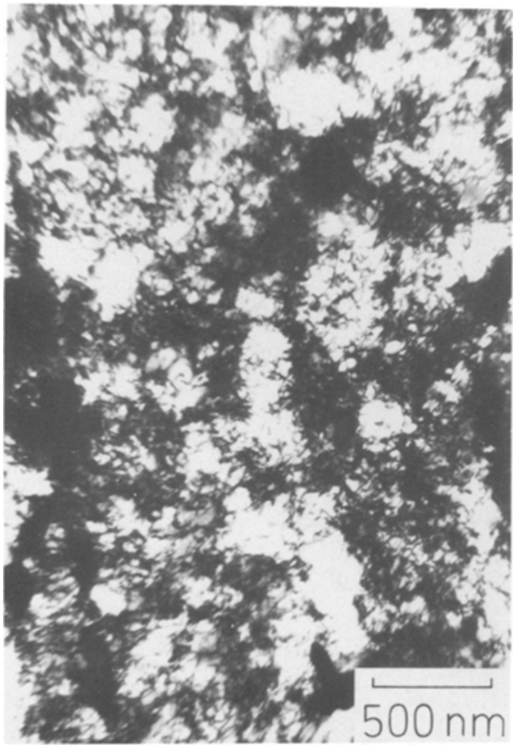

Figure 19 Thin foil from accelerated creep test specimen, showing very high dislocation density.

4.3. Embrittlement

A small selection of results from the mechanical test programme carried out on these steels by BNL is presented in Tables V to VII. While the tensile tests clearly demonstrate a process of embrittlement, the creep test data is less positive, particularly for the thicker specimens. That the embrittlement is not a simple, bulk phenomenon, as it was at first considered, is confirmed by the results of a study of preparation method effects (Table VII) and the bend test experiments. Consideration of the BNL results and the results presented here suggest that not only is there a true bulk embrittlement effect but that there is also a surface phenomenon acting, although the two effects are not additive. This is demonstrated by the absence of embrittlement from unaged material in creep tests, although prepared in the same fashion.

It has not proved possible to positively identify the cause of the bulk embrittlement although it seems that the very dense $M_{23}C_6$ precipitation is the most likely cause. The dense intragranular precipitation would impede dislocation movement and reduce ductility. The very dense intergranular precipitation could lead to grain boundary stresses as a result of volume changes on precipitation or different thermal expansion coefficients. Certainly strain has been observed near grain boundaries. Lattice mismatches between matrix and precipitates might weaken the boundaries and grain

TABLE V Creep tests on strip specimens

Specimen	Thickness (mm)	Test temperature (° C)	Stress (MN m^{-2})	Strain rate (sec^{-1})	Failure time (sec)	Overall strain (%)
A (28 000 h)	0.75	650	151.7	1.21×10^{-8}	5.1×10^{6}	34.1
			125.0	3.0×10^{-10}	2.08×10^{7}	20.7
			103.4	6.0×10^{-10}	3.32×10^{7}	34.1
Typical 316	0.75	650	151.7	1.68×10^{-7}	1.38×10^{6}	71.5
			125.0	4.0×10^{-8}	5.97×10^{6}	67
			103.4	4.6×10^{-9}	2.95×10^{7}	32
A (28 000 h)	3.0	650	225	1.8×10^{-7}	1.07×10^{6}	45.9
Typical 316	3.0	650	230	1.9×10^{-7}	6.01×10^{5}	45

boundary sliding, necessary during deformation, would be made more difficult.

The surface embrittlement effect probably results from an interaction between a high dislocation density in the surface, produced by work hardening, and a high precipitate density, produced by ageing. The combination produces a very hard surface layer which is more resistant to deformation than the bulk material and thus when strained the weak grain boundaries at the surface would fail. The effect would be absent from the solution-treated material because the dislocations in the surface layers could move easily, not being blocked by precipitates.

5. Conclusions

It has been shown that the long-term thermal ageing of commercial type 316 steel produces a very complex microstructure. To obtain a detailed knowledge of this microstructure it is advantageous to use as wide a range of techniques as possible.

Thermal ageing also has the effect of changing the mechanical properties of type 316 steel. In particular the material is embrittled. However, it is important to note that this is not a consequence of the formation of sigma phase but most likely arises from very dense precipitation of $M_{23}C_6$ on the grain boundaries. This particular mode of embrittlement also makes the material very sensitive to work hardening effects which, if thin, strip-type specimens are used for mechanical testing, can considerably complicate the mechanical behaviour. Thus, it is important that if thin strip specimens must be used, because of a lack of material for instance, they should be prepared with great care so as to avoid all possibility of complicating surface effects.

TABLE VI Tensile tests at 625° C in air

Specimen	Overall strain (%)	Ultimate tensile strength (MN m^{-2})	0.2% proof stress (MN m^{-2})
A (28 000 h)	9.8	335	241
B (60 000 h)	13.4	376	264
C (re-solution) treated)	34.7	297	138
Typical virgin 316	35	300	100–150

The industrial implications of this extreme sensitivity of aged material to work hardening of the surface are not clear. It is probably relatively unimportant since most industrial components would be sufficiently large to make surface effects insignificant. A possibility exists however that repair of aged components, which work hardens the surface, might lead to grain-boundary cracking of the surface. This might result in nucleation of larger, bulk cracking or a considerably increased rate of stress corrosion cracking.

It is of interest to note that the creep mechanisms are probably different for accelerated creep test conditions and service conditions. Thus, accelerated creep test data should be treated with care when considering the possible behaviour of material under service conditions.

TABLE VII

Preparation method	Ultimate tensile strength (MN m^{-2})	0.2% proof stress (MN m^{-2})	Overall strain (%)
Punched out from serviced material	335	241	9.8
Punched out and then re-solution treated	417	121	31
Prepared by careful filling	393	171	18.1

Acknowledgements

I am grateful to the CEGB for providing the specimens and for making their results available to me. I would like to thank Dr J. A. Eades and Dr J. W. Steeds, of Bristol University and Dr P. Marshall of CEGB Berkeley Nuclear Laboratories for their useful discussions and advice, and the Science Research Council for financial assistance.

Appendix Estimates of strain rates

For Herring–Nabarro creep,

$$\dot{\epsilon} = \frac{10\sigma D_L \Omega}{(GS)^2 kT}, \qquad \text{(A1)}$$

where Ω is the vacancy volume, $\dot{\epsilon}$ is the strain rate, σ is the applied stress, D_L is the diffusion coefficient, (GS) is the average grain diameter, k is Boltzmann's constant and T is absolute temperature.

For Coble creep,

$$\dot{\epsilon} = \frac{150\sigma D_B w \Omega}{(GS)^3 kT}, \qquad \text{(A2)}$$

where $\dot{\epsilon}$, σ, Ω, (GS), k and T are as given for Equation A1. D_B is the grain boundary diffusion coefficient and w is the width of the grain boundary.

For dislocation creep,

$$\dot{\epsilon} = A\sigma^n \exp\left(\frac{-Q}{kT}\right), \qquad \text{(A3)}$$

where $\dot{\epsilon}$, σ, k and T are as given for Equation A1, A and n are constants and Q is the activation energy.

No diffusion data for type 316 steel could be found so data for a 20Cr/25Ni/Nb steel [9, 10] was used. This would probably not be very different for type 316 steel and is good enough for order of magnitude calculations.

For bulk diffusion the data for chromium was used since this gave the largest coefficient compared with iron and nickel and for grain boundary diffusion an average of the data was used since the values for Fe, Cr and Ni were similar. Using the data and the equations

$$D_L = D_{L_0} \exp\left(\frac{-Q_L}{RT}\right) \qquad \text{(A4)}$$

$$D_B w = D_{B_0} w \exp\left(\frac{-Q_B}{RT}\right) \qquad \text{(A5)}$$

the diffusion coefficients at 650° C were calculated to be

$$D_L = 2.24 \times 10^{-19}\,\mathrm{m^2\,sec^{-1}}$$

and

$$D_B w = 5.72 \times 10^{-24}\,\mathrm{m^3\,sec^{-1}}.$$

The average grain size was determined by etching and optical microscopy to be approximately 30 μm. The vacancy volume was taken as $1.17 \times 10^{-29}\,\mathrm{m^3}$. These values were then used to calculate the strain rates arising from diffusion creep mechanisms.

For dislocation creep, Equation A3 was reduced to

$$\dot{\epsilon} = B\sigma^n, \qquad \text{(A6)}$$

where $B = A\exp(-Q/kt)$, and the data from the accelerated creep tests (Table VI) were used to calculate B and n since the tests were conducted at the appropriate temperature of 650° C. The values obtained were

$$n = 9.4$$

and

$$B = 2.20 \times 10^{-84}.$$

The value for n was considered to be too high and it was decided to use a more typical value of $n = 7$. This gave $B = 9.39 \times 10^{-65}$. Using these values the expected creep rate at 36 MN m^{-2} and 650° C was calculated.

References

1. K. E. COOKE, N. EVANS, L. STOTER and J. W. STEEDS, Proceedings of the Electron Diffraction 1927–77, Institute of Physics Conference Series No. 41 (Institute of Physics, Bristol, 1977).
2. N. EVANS, PhD thesis, Bristol University (1981).
3. J. K. LAI and A. WICKENS, *Acta. Met.* 27 (1979) 217.
4. J. E. SPRUIELL, J. A. SCOTT, C. S. ARY and R. L. HARDIN, *Met. Trans.* 4 (1973) 1533.
5. B. WEISS and R. STICKLER, *ibid.* 3 (1972) 851.
6. P. R. HOWELL, J. O. NILSSON and G. L. DUNLOP, *Phil. Mag.* 38 (1978) 39.
7. C. HERRING, *J. Appl. Phys.* 21 (1950) 437.
8. R. L. COBLE, *ibid.* 34 (1963) 1679.
9. A. F. SMITH and G. B. GIBBS, *Met. Sci.* 3 (1969) 93.
10. *Idem, ibid.* 2 (1968) 47.

Received 2 July and accepted 3 October 1980.